The evolution of internal waves in a rotating, stratified, circular basin and the influence of weakly nonlinear and nonhydrostatic accelerations

Alberto de la Fuente
Departamento de Ingeniería Civil, Universidad de Chile, Santiago, Chile

Kenji Shimizu, and Jörg Imberger[1]
Centre for Water Research, The University of Western Australia, Crawley, 6009, Western Australia, Australia

Yarko Niño
Departamento de Ingeniería Civil, Universidad de Chile, Santiago, Chile

Abstract

The evolution of internal waves in a two-layer rotating circular lake was studied under nonlinear and weak nonhydrostatic effects. Inclusion of nonlinear acceleration allowed the waves to steepen at the rear of the crest in deep lakes, forming a front with time. The nonhydrostatic acceleration is shown to counteract this wave steeping, leading to wave dispersion, and when the two effects are in balance, solitary-type waves can form. It is shown that a Kelvin wave evolves by imparting energy primarily to submodes of the parent cyclonic wave by steepening and to solitary-type waves. By contrast, a Poincaré wave is shown to evolve without shedding much of its energy to other waves, and only a small fraction of the wave energy goes to other submodes, and this is not lost from the parent wave but rather is periodically transferred back into the parent wave. When both Kelvin and Poincaré waves were present simultaneously in the waterbody, then an interaction was observed when both waves were in phase, which gave rise to additional wave components.

A common conceptual model, used to study motion in stratified lakes (Fischer et al. 1979), is to simplify the stratification into two, three, or more layers; this provides a good approximation to the basin-scale internal waves modes up to the number of fluid layers (Mortimer 1952; Monismith 1985; Munnich et al. 1992). With this assumption, the energy imparted by the wind enters the surface layer and is then progressively distributed into the layers below as the baroclinic pressure field sets up motions in the lower layers (Imberger 1998; Wüest and Lorke 2003).

The interfacial response due to a surface shear stress, in a non-rotating waterbody, was described by Spigel and Imberger (1980), who extended the earlier analytic solution developed by Heaps and Ramsbottom (1966). These authors showed that, along the fetch, the steady-state equilibrium could be described by a constant interfacial slope $\partial_x \eta_2 = -\bar{h}_1 (LW)^{-1}$, in which the minus sign signifies that the slope is in the opposite direction to the

imposed wind stress and η_2 is the interfacial displacement with respect to the unforced equilibrium, L is the length of the basin, $\bar{h}_1$ is the equilibrium top layer thickness, ∂_x is the partial differential operator with respect to x, and

$$W = \frac{g' \bar{h}_1^2}{u_*^2 L} \tag{1}$$

is the Wedderburn number. In Eq. 1, $g' = g \rho_0^{-1} (\rho_2 - \rho_1)$ is the reduced gravity, ρ_1 and ρ_2 are the layer densities, ρ_0 is the reference density, g is the acceleration due to gravity, and u_* is the shear velocity at the water surface. From this, it follows immediately that the maximum nondimensional displacement $(\eta_{2\,max}/\bar{h}_1)$, is equal to $(2W)^{-1}$; $W = 0.5$ is thus the condition for full upwelling of the bottom water (Thompson and Imberger 1980; Imberger and Hamblin 1982). The interfacial setup is achieved via internal waves initiated at both the upwind and downwind boundaries, propagating toward the interior, and arriving at the center of the lake one quarter of an internal period T_i later (Mortimer 1952; Spigel and Imberger 1980):

$$T_i = \frac{2L}{c_0} \tag{2}$$

where

$$c_0 = \sqrt{g' \frac{\bar{h}_1 \bar{h}_2}{\bar{h}_1 + \bar{h}_2}} \tag{3}$$

is the internal wave celerity and $\bar{h}_2$ is the equilibrium bottom layer thickness (Mortimer 1952). Under the linear

theory assumption, these waves keep propagating back and forth across the length of the lake with a period T_i. For motions initiated from an initial interface displacement, it is convenient to define the Wedderburn number by (Horn et al. 2001)

$$W = \frac{\bar{h}_1}{2\eta_0} \tag{4}$$

where η_0 is the initial maximum displacement.

For a lake large enough that the time a wave takes to propagate across the basin $(T_i/2)$ is similar to or longer than the time it takes the lake to turn through $360°$, $(2f)^{-1}$ (where f is the Coriolis parameter), the waves will obviously be strongly influenced by the Earth's rotation. The ratio of these two times is generally known as the Burger Number (Gill 1982; Antenucci et al. 2000).

$$S = \frac{4}{T_i f} \tag{5}$$

Two major classes of waves are possible for such rotating basins. First, Kelvin, or cyclonic waves, in which the forces balance in the direction of propagation, remains the same as for nonrotating waves. The motion is essentially unidirectional and the Coriolis acceleration, induced by this unidirectional motion, is balanced by an oscillating transverse pressure gradient. Second, Poincaré or anticyclonic waves, in which the Coriolis acceleration induces a motion normal to the pressure gradient, causes anticyclonic rotation of the interface displacement and fluid velocity with nearly circular particle paths. For a particular basin geometry, horizontal modes can be decomposed into multiple fundamental modes oscillating in harmony side by side (Gómez-Giraldo et al. 2006). In simple terms, those modes are excited that match the spatial and temporal distribution of the imposed wind stress (Csanady 1973; Gómez-Giraldo et al. 2006; Shimizu et al. 2007).

The influence of the nonlinear inertia acceleration has been investigated in some detail in the absence of rotation. Advective acceleration leads to steepening of an initial basin-scale wave (Ripa 1982; Horn et al. 2001; Boegman et al. 2005a) over a characteristic time T_s, defined by Horn et al. (2001).

$$T_s = \frac{L}{\alpha \eta_0} \tag{6}$$

$$\alpha = \frac{3}{2} c_0 \frac{\bar{h}_2 - \bar{h}_1}{\bar{h}_2 \bar{h}_1} \tag{7}$$

Steepening is followed by convective overturning (Federov and Melville 1995) and degeneration into solitons (Grimshaw et al. 1998; Horn et al. 2001; Boegman et al. 2003). The nonlinear acceleration also causes transfer of energy to higher basin-scale modes (Maxworthy 1983; Melville et al. 1989; Fedorov and Melville 2000) and energy transfers to and from background currents (Clark and Imberger 1996; Riley and Lelong 2000).

Studies in an infinite domain have not shown whether waves of permanent form, such as solitons in the nonrotating case, exist for the rotating case (Grimshaw et al. 1998; Helfrich 2007). Periodic growth of solitary-type waves and their subsequent destruction in a rotating stratified fluid have been discussed by Grimshaw et al. (1998) and Helfrich (2007). Previously, steepening of Kelvin waves in a rotating straight channel had been shown by Bennett (1973) and Fedorov and Melville (1995), and Renouard et al. (1986) had also demonstrated the formation of solitary-type waves with a stable longitudinal shape described by a squared hyperbolic secant (sech²) profile. However, the degeneration of basin-scale waves in a rotating enclosed basin does not appear to have been investigated.

The main objective of this study is to improve the understanding of the nonlinear steepening and nonhydrostatic wave dispersion on the propagation of basin-scale internal waves in a two-layer, stratified, rotating enclosed circular basin. A circular basin was chosen because analytic solutions for the linear regime are available. The characteristic numbers, such as W, T_i, S, and T_s, are combined to provide a parameter space in which to discuss the analytical and numerical results for the cases of a spatially uniform, suddenly-imposed wind forcing and the free evolution of the Kelvin, Poincaré, or both types of waves.

The paper is organized as follows. First, the analytic solution for a circular basin with a two-layer stratification, rederived by Stocker and Imberger (2003), is revisited to understand the general features of the solution and to display scaling that captures the motion. Then, the n-layer model, used in this study (de la Fuente et al. 2006), is described briefly. This is followed by the derivation of the solution for a suddenly imposed wind on an n-layer fluid in a circular basin and the free evolution from initial interface displacement. The condition that defines the formation of solitary-type waves and transfer of energy from initial basin-scale waves to submodes and solitary-type waves is then presented.

Linear approximation and scaling—Modal decomposition of the linear momentum and mass equations for an n-layer system in a rotational frame of reference reduce to a set of n-linear, independent, vertical modal equations, the solutions of which are described by equations equivalent to the shallow-water equations for a homogeneous basin (Csanady 1968; Monismith 1985; Antenucci and Imberger. 2001). For a circular homogeneous basin with a two layer stratification, forced by a suddenly imposed, spatially uniform shear stress, Stocker and Imberger (2003) showed that the flow velocities and vertical displacements of the interface were linear functions of the inverse of the Wedderburn number. Therefore, it is advantageous to scale the vertical interfacial displacements η_2 and layer-averaged horizontal velocities u_i so that

$$\eta_2^* = 2W \frac{\eta_2}{\bar{h}_1} \qquad u_i^* = 2W \frac{u_i}{c_0} \tag{8}$$

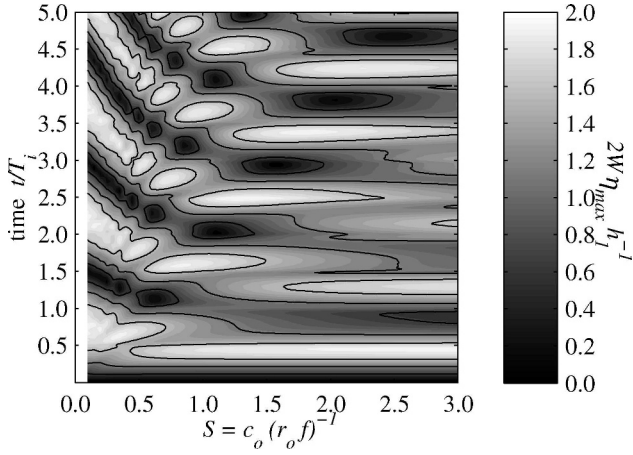where the asterisk denotes nondimensional variables, W is the Wedderburn number with $L = 2r_0$ for circular basins

Fig. 1. Maximum interfacial displacement as a function of time and Burger number (S). Displacement and time were nondimensionalized as in Eq. 8 and by the internal period T_i, respectively.

Fig. 2. (A) Time series of nondimensional surface rate of work by or to the wind. (B) The nondimensional total energy of the lake, TE* (solid line), and its partitioning between total kinetic energy, TKE*, and total available potential energy, TPE* (dotted and dashed lines, respectively), for $S = 0.5$. Shaded areas show periods when wind takes energy from the lake. The rate of working and energies were nondimensionalized as in Eq. 9.

(Eq. 1), and the radius and time are nondimensionalized with respect to the radius of the basin r_0 and the internal wave period T_i (Eq. 2 with $L = 2r_0$), respectively. This scaling allows the forcing to be removed from the equations, leaving only the Burger Number and the ratios of layer thicknesses as parameters.

The maximum interfacial displacements were computed according to this analytic solution for different values of S and the time t^*, as is shown in Fig. 1. When the Burger Number S is large, both the Kelvin and Poincaré waves have the same wave shape and angular frequency, but they rotate in opposite directions. Superposition of such matching waves results in a fundamental standing internal wave mode, as previously discovered by Antenucci and Imberger (2001). The maximum displacements are produced first at $t = 0.42T_i$, when the radial Kelvin and Poincaré waves are in phase for the first time; this occurs periodically every $0.84T_i$. For medium rotation ($S \approx 0.5$), Kelvin and Poincaré waves have similar amplitudes and still produce the first local maximum when they become in phase at about $t = T_i/2$ (see Fig. 1); however, this maximum displacement does not occur at the upwind end because the troughs of the two waves are displaced progressively as S decreases because of the differences in their natural periods. In the limit of small Burger Numbers, the Kelvin wave dominates the response and the timescales of the problems given by the period of the fundamental mode Kelvin wave, T_k, which can easily be computed by the polynomial fit presented by Antenucci and Imberger (2001). For winds that have a duration longer than T_i or T_k, the amplitudes show a periodic behavior with maximum amplitudes itself oscillating because natural angular frequencies of the modes do not occur in multiples of the fundamental mode frequency.

In Fig. 2, we show the total nondimensional energy of all the wave components, partitioned into kinetic and available potential energy and work done by wind. The nondimensionalization used for the different energy bins was derived from the scaling introduced in Eq. 8 such that
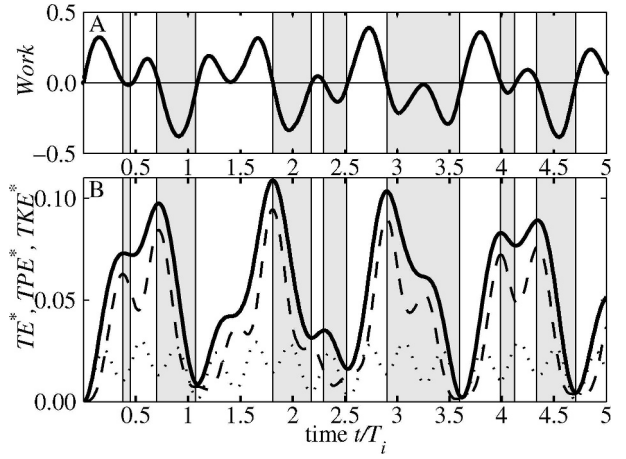
$$\text{TKE}^* = \frac{2W}{c_0\rho_0 u_*^2 \Omega L}\text{TKE} \qquad \text{TPE}^* = \frac{2W}{c_0\rho_0 u_*^2 \Omega L}\text{TPE}$$

$$\text{TE}^* = \frac{2W}{c_0\rho_0 u_*^2 \Omega L}\text{TE}$$
(9a)

$$\text{Work}^* = \frac{2W}{c_0\rho_0 u_*^2}\int_\Omega \vec{\tau}_s \vec{u_1}\, d\Omega$$
(9b)

where TKE*, TPE*, and TE* are the kinetic, available potential, and total energy, respectively, integrated over the basin, Work* is the work done by wind over the surface, and Ω is the surface area.

For wind durations shorter than $T_i/2$ or $T_k/2$, the wind does work on the lake, exciting the internal waves. The supplied energy is primarily transferred to available potential energy (about 75% of the total energy for weak rotation and 50% for strong rotation). On the other hand, during the second half of the period, the existing waves do work on the wind because the direction of the wind now opposes that of the surface velocity associated with the wave. The wind thus periodically energizes and cancels the internal seiches. The transfer to available potential energy is less efficient under strong rotation in that the solution, for that limit, is a pure Kelvin wave, which has an equi-partitioning between kinetic and available potential energy, whereas in the limit of weak rotation, the solution approaches that for a nonrotating internal seiche, which has the property that the energy is maximum when all the energy is either all potential or all kinetic.

Governing equations and numerical scheme—The standard shallow-water equations with the Boussinesq approximation and with the assumption of hydrostatic pressure can be derived for an *n*-layer stratification by vertically

integrating the full equations of motion between $z = z_{i+1}$ to $z = z_i$, where z is the vertical coordinate, and z_{i+1} and z_i correspond to the bottom and upper interfaces that define the ith layer, respectively (Baines 1998). The three governing equations for each layer can be written as

$$\frac{\partial U_i}{\partial t} + \frac{\partial F_i^x}{\partial x} + \frac{\partial F_i^y}{\partial y} = H_i \qquad (10)$$

where

$$U_i = [h_i, u_i h_i, v_i h_i]^T \qquad (11a)$$

$$F_i^x = \begin{pmatrix} u_i h_i \\ u_i u_i h_i \\ u_i v_i h_i \end{pmatrix} \qquad F_i^y = \begin{pmatrix} v_i h_i \\ v_i u_i h_i \\ v_i v_i h_i \end{pmatrix} \qquad (11b)$$

and

$$H_i = \begin{pmatrix} 0 \\ -h_i g \sum_{j=1}^{i} \varepsilon_j \frac{\partial z_j}{\partial x} + \frac{\tau_i^x}{\rho_0} - \frac{\tau_{i+1}^x}{\rho_0} + f v_i h_i \\ -h_i g \sum_{j=1}^{i} \varepsilon_j \frac{\partial z_j}{\partial y} + \frac{\tau_i^y}{\rho_0} - \frac{\tau_{i+1}^y}{\rho_0} - f u_i h_i \end{pmatrix} \qquad (11c)$$

where ρ_i, u_i, and v_i are the layer-averaged density and velocities in x and y directions, respectively, τ_i^x and τ_{i+1}^x are the upper and bottom interfacial shear stresses in the x direction, and $\rho_0 \varepsilon_i = (\rho_i - \rho_{i-1})$ for $i > 1$ and $\rho_0 \varepsilon_1 = \rho_1$ for $i = 1$.

These equations were solved by the MUSCL–Hancock method for hyperbolic equations of an n-layer system (Bradford et al. 1997; Loose et al. 2005) (*see* Web Appendix 1, www.aslo.org/lo/toc/vol_53/issue_6/2738a1.pdf, for the details). Benchmarks that validate the numerical scheme were presented by de la Fuente et al. (2006). Because the equations assume an inviscid fluid, shear stresses were only considered at the water surface, and at the side walls, it was assumed that no fluid crosses, but slip was allowed.

The weak nonhydrostatic effects were included in the model proposed by Brandt et al. (1997), who kept the terms of the order $\mu^2 = h^2 L^{-2}$, but neglected the terms of the order $\varepsilon = a h^{-1}$, where a is the wave amplitude scale and h and L are the layer thickness and basin scale, respectively. With this simplification, the nonhydrostatic terms in the momentum equations for each layer can be included as follows:

$$\frac{\partial \overrightarrow{u_i} h_i}{\partial t} = B_i \overrightarrow{\nabla} \left[\frac{\partial}{\partial t} \left(\nabla \cdot \overrightarrow{u_i} h_i \right) \right] + \overrightarrow{A} \qquad (12)$$

where

$$B_i = \begin{cases} \frac{h_1^2}{6} & i = 1 \\ \frac{h_2^2}{3} + \frac{h_1 h_2}{2} & i = 2 \end{cases} \qquad (13)$$

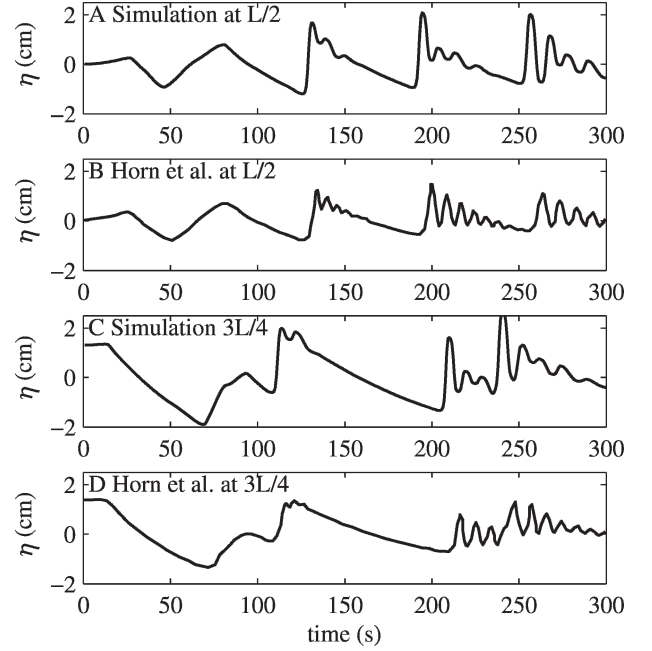and $\overrightarrow{A}$ is the vector containing all the F_i and H_i terms of

Fig. 3. Comparison of interfacial displacement between simulation and experimental results in a two-layer, nonrotating channel of length L. (A, C) Simulations and (B, D) experiments by Horn et al. (2001). The waves were generated by initial linear tilt, and resulting interfacial displacement was measured at $L/2$ and $3L/4$.

Eqs. 11B,C. The nonhydrostatic terms of Eq. 12 were solved numerically according to the method described in Web Appendix 1. The above approximation includes the assumption that h_1 and h_2 are constant in the conservation of volume calculations (Eq. 12) (Tomasson and Melville 1992). However, as explained in Web Appendix 1, the final scheme adopted here uses $h_i + \eta$ in place of h_i because it simplified the numerical scheme. The model results were then compared with the experimental data from Horn et al. (2001) for waves steeping in a nonrotating rectangular channel; the model successfully reproduced the essential features such as number and shape of solitary waves and timing of their emergence (Fig. 3). Although the amplitudes of solitary waves and the propagation velocity showed some deviations from the experimental data because of neglect of viscous damping (Horn et al. 2002), they do not pose severe limitations for our analyses in that we focus on the inviscid dynamics.

Interaction of internal waves and the imposed wind stress forcing the motion—The model, once validated, was applied to the case of a suddenly imposed wind over a circular basin containing a two-layer stratification. The effects of the weak nonlinearity and the inclusion of weak nonhydrostatic accelerations can be seen in Fig. 4, where this model solution is compared with the linear solution for the case $S = 0.5$, $W = g' \bar{h}_1^2 (u_*^2 2 r_0)^{-1} = 1.83$, and $\bar{h}_1 / \bar{h}_2 = 1.0$; the forcing was strong enough to induce nearly full upwelling at the first overshoot at $t \approx T_i / 2$. The trend of the kinetic, available potential, and total energy were similar to the linear solution, although the nonlinea-
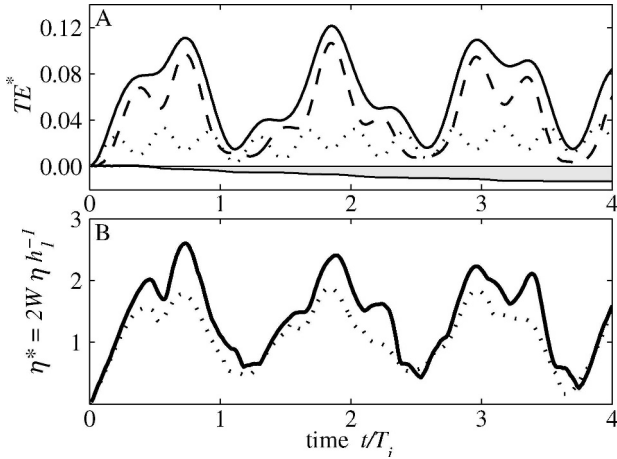
Fig. 4. Comparison between simulation and analytic results for $S = 0.5$, $W = 2.3$, and $\bar{h}_1 = \bar{h}_2$. (A) Time series for the total energy and its partitioning between kinetic and available potential energies. Shaded area shows the estimated numerical dissipation of the simulation. (B) Linear (solid line) and nonlinear (dotted line) time series of the maximum interfacial displacement.

rities allowed the wind to impart slightly more total energy to the motion (Fig. 4A), which is also reflected in the nondimensional interface displacement. Energy losses because of numerical dissipation were found to be <10% of the total energy, for the duration of the simulation (Fig. 4A). Throughout this paper we assume that the kinetic energy due to the vertical velocity is two orders of magnitude smaller than the potential energy plus kinetic energy that is due to horizontal velocities, and may thus be neglected.

The well-known effect of the layer depth ratio on the nonlinear steepening (Horn et al. 2001) is shown in Fig. 5, where the interfacial displacements, at the upwind end and at the center of the basin, are shown for the depth ratios $\bar{h}_1/\bar{h}_2 = 1.0$ and 0.1, with the same Burger and Wedderburn numbers as before. When the layer thicknesses were
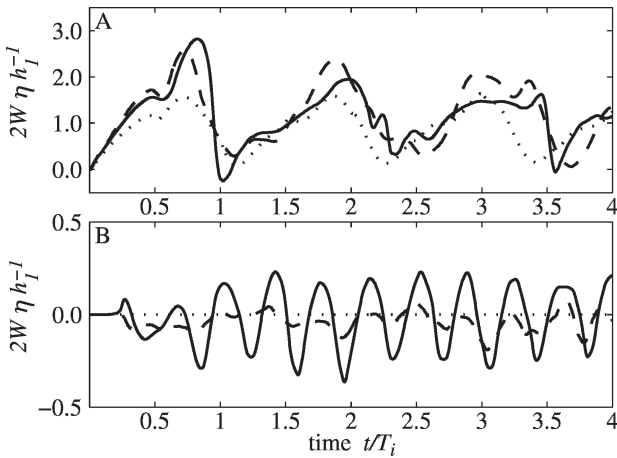

Fig. 5. Time series of nondimensional interfacial displacement for the linear case (dotted line) and nonlinear and weak nonhydrostatic cases for $\bar{h}_1/\bar{h}_2 = 1.0$ (dashed line) and 0.1 (solid line). (A) At the upwind end and (B) at the center of the basin. $S = 0.5$ and $W = 1.83$.

equal, the inclusion of the nonlinear and nonhydrostatic terms amplified the interfacial displacements, compared with those from the linear solution, almost symmetrically. However, for the small depth ratio, $\bar{h}_1/\bar{h}_2 = 0.1$, the waves steepened more at the rear of the crest (Choi and Camassa 1999). Furthermore, at the center of the basin, an almost stationary interface oscillation was observed to appear with a period of about $T_i/3$ (Fig. 5B). The amplitude of this displacement was much less for the simulation with $\bar{h}_1/\bar{h}_2 = 1.0$ than for $\bar{h}_1/\bar{h}_2 = 0.1$.

The expected generation of solitary-type waves because of steepening of the Kelvin wave is not observed, as seen in Fig. 5A. The interaction between the wind and the waves modulated the total energy as discussed above. The steepening timescale, Eq. 6, defines when the nonlinear effects become important for free oscillations with constant energy in time (Horn et al. 2001). The suddenly imposed wind problem analyzed here, however, imposes temporal changes on the total energy with the timescale characterized by T_i or T_k. The ratio between these two timescales,

$$\frac{T_s}{T_i} = \frac{1}{3\eta_0}\frac{\bar{h}_1\bar{h}_2}{\bar{h}_2 - \bar{h}_1} \qquad (14)$$

should indicate whether there is enough time to produce steepening before the energy available for steepening is extracted by the wind. To test this hypothesis, simulations were carried out for $S = 0.5$ and $T_s/T_i = 0.40$, 0.48, 0.88, and 1.29, and the results are shown in Fig. 6. The first case considers $\bar{h}_1/\bar{h}_2 = 0.05$ and $W = 1.83$, the second and fourth cases were run with $\bar{h}_1/\bar{h}_2 = 0.1$ and $W = 1.83$ and 3.66, respectively, whereas the third case was conducted with $W = 1.83$ and $\bar{h}_1/\bar{h}_2 = 0.55$. To calculate T_s/T_i, η_0 was taken as the maximum interfacial displacement at $t \approx T_i/2t$. Note that the smaller ratios T_s/T_i are closer to the smaller possible value of 0.3 for the limit $\bar{h}_1 \ll \bar{h}_2$ and $\eta_0 \to \bar{h}_1$. Figure 6H shows the total energy as a function of time, indicating three maxima at approximately $t/T_i = 0.75$, 1.8, and 2.9, respectively.

The three runs in which $T_s < T_i$ (darkest lines) show steepening of the rotating internal waves that were modulated by energy extraction by the wind. The results for $T_s/T_i = 0.40$ and 0.48 (dotted and dashed lines) show the energy peaking after the second maximum in total energy (Fig. 6E), but this recedes as the wind drains the energy from the basin-scale wave before solitary-type waves can form (Fig. 6F). The magnitude of the steepening in Fig. 6E is larger for $T_s/T_i = 0.40$ than $T_s/T_i = 0.48$. A similar behavior was observed for $T_s/T_i = 0.88$ (solid dark line), whereas the results for $T_s/T_i > 1$ (light solid line) did not show any steepening at all.

Free evolution of individual Kelvin and Poincaré waves— The evolution of the monochromatic Kelvin and Poincaré wave was also analyzed with the model by initializing the simulations with the velocity and displacement field from the linear solutions (Eq. 12). The interface displacements from simulations for the initial Kelvin wave case, with an amplitude equivalent to a Wedderburn number
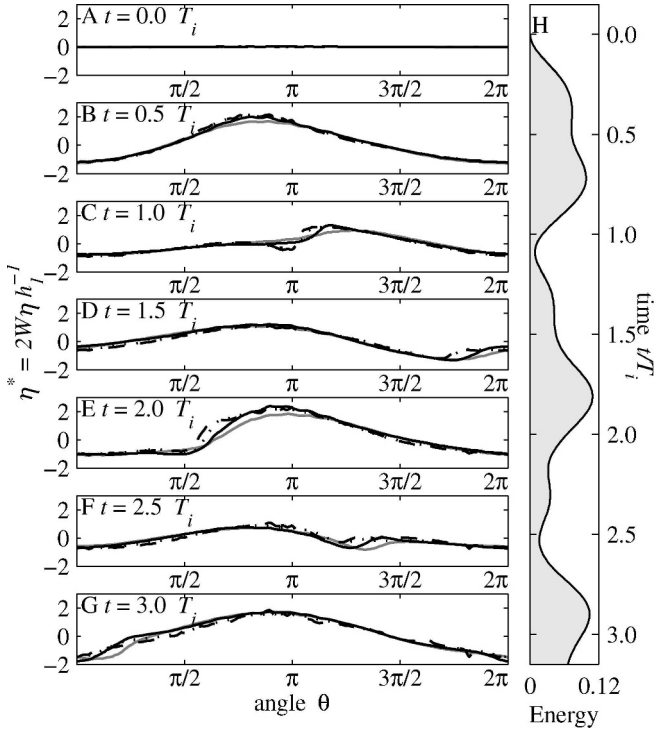
Fig. 6. (A–G) Azimuthal profiles of the interfacial displacement for simulations of the spatially uniform, suddenly imposed wind problem in a circular basin for ratios $T_s/T_i = 0.40, 0.48, 0.88$ (dashed, dotted, and solid dark lines, respectively), and 1.29 (light solid line) from $t = 0$ to $t = 3T_i$, with a $0.5T_i$ interval. (H) The time series of the total energy shown in Fig. 2, oriented along the vertical direction from top ($t = 0$) to bottom ($t = 3T_i$).

$W = \bar{h}_1(2\eta_0)^{-1} = 0.6$, $\bar{h}_1/\bar{h}_2 = 0.1$, and three Burger Numbers are shown in Figs. 7, 8. The steepening of the rear of the crest of the linear wave commences at approximately $t = T_s$ ($t' = 1.0$); degeneration into a train

of solitary-type waves followed shortly after this time in all the cases. When the nonhydrostatic term was switched off, the initial basin-scale wave kept steepening until it formed a steep front, confirming the well-known fact that the formation of solitary-type waves requires the pressure dispersion term (Fig. 8A,B). For a given value of S, the following features, similar to solitary waves in nonrotating flows (Grimshaw, et al. 1998; Ostrovsky and Stepanyants 2005; Helfrich and Melville 2006), were used to identified the presence of the solitary-type waves: (1) The azimuthal scale (wavelength) increased with the Wedderburn number, as in nonrotating cases in which larger solitons have shorter wave lengths (compare, e.g., Fig. 8A,C,E). (2) The azimuthal shape of the solitary-type waves closely follows the squared hyperbolic secant profile for smaller ratios $\bar{h}_1/\bar{h}_2$ but turned into hyperbolic tangent profiles for relatively deeper surface layers (e.g., compare solid and dashed lines in Fig. 8B with the squared hyperbolic secant and hyperbolic tangent profiles in Fig. 8H, respectively). This is well known and follows when higher order terms are included in the KdV equation (Lee and Beardsley 1974; Ostrovsky and Stepanyant 2005; Helfrich and Melville 2006). (3) As is known from KdV theory, when the second-order terms are included (Lee and Beardsley 1974), the amplitude is limited, leading to a maximum amplitude. This amplitude is proportional to the magnitude of the initial perturbation and is a function of $\bar{h}_1/\bar{h}_2$ (Fig. 8G). Note that, although these waves are not true solitons described by the permanent squared hyperbolic secant shape, they retain their form over simulated time ($3T_s$), large compared with the travel time across a lake, and they can break at the coast and dissipate their energy.

On the other hand, the results differed from the nonrotating case because the effects of the Earth's rotation modified the maximum amplitude of these solitary-type waves (Fig. 8G), in which smaller S (strong rotation) is associated with smaller amplitudes.
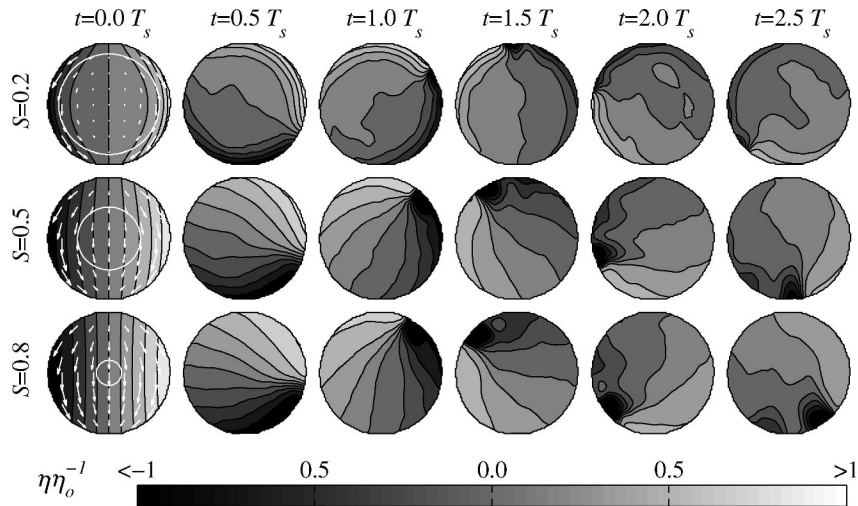

Fig. 7. Evolution of the interfacial displacement with the nonhydrostatic terms for an initial monochromatic Kelvin wave for $W = \bar{h}_1(2\eta_0)^{-1} = 0.6$. White circle on initial conditions shows the Rossby radius measured from the shore, and white arrows are the layer-averaged velocity in the upper layer. The waves rotate anticlockwise, as in the northern hemisphere $t' = t/T_s$.
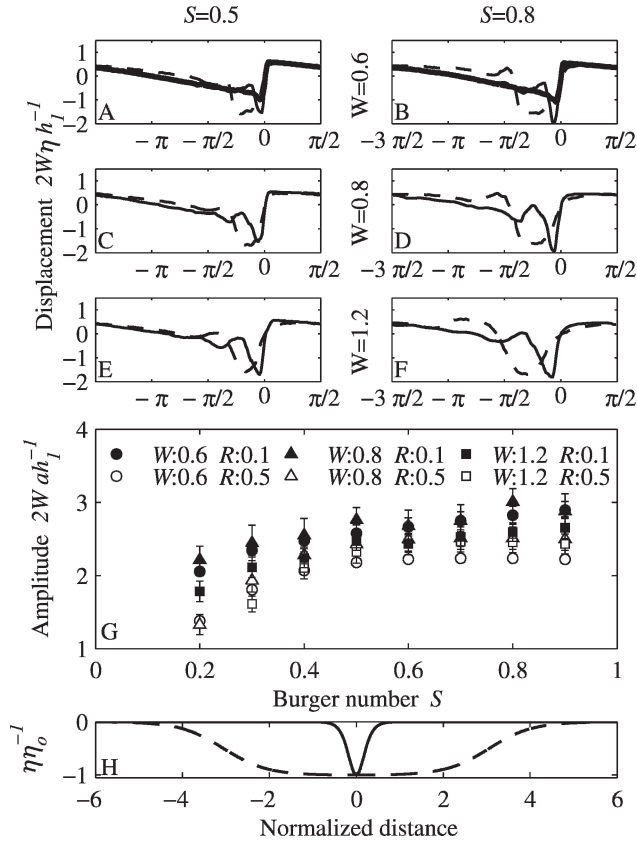
Fig. 8. (A–F) The azimuthal profiles of the interfacial displacement at $t = 1.5T_s$; $r = r_0$ for $W = \bar{h}_1 (2\eta_0)^{-1} = 0.6$, 0.8, and 1.2; ratio $\bar{h}_1 / \bar{h}_2 = 0.1$ (solid line) and 1.0 (dashed line); and $S = 0.5$ (first column) and 0.8 (right column). Thick lines in panels A and B show the hydrostatic solution. (G) Temporal average amplitude of solitary-type waves a as a function of S for $W = \bar{h}_1 (2\eta_0)^{-1} = 0.6$, 0.8, and 1.2, and $R = \bar{h}_1 / \bar{h}_2 = 0.1$ and 0.5. Note that the vertical axis is the amplitude normalized by initial perturbation displacement since $2W a \bar{h}_1^{-1} = a/\eta_0$. (H) The squared hyperbolic secant shape of the first-order KdV equation (solid line) and hyperbolic tangent shape of the second-order KdV equation (dashed line).

Interestingly, the evolution of an initial Poincaré wave showed significant difference from the Kelvin wave cases (Fig. 9). Nonlinear steepening produced fronts steeper than those for the Kelvin wave. However, this did not lead to subsequent degeneration into solitary-type waves, as described for the Kelvin waves (compare Figs. 7, 9). The fronts appeared and disappeared periodically, which modulated the wave structure but did not change the amplitude and basic structure of the initial Poincaré wave significantly (*see* subsequent section). The inclusion of the nonlinear terms was necessary for the steepening, but the results were almost insensitive to the inclusion of the nonhydrostatic term.

Redistribution of energy—The energy contained in the steepened waves and solitary-type waves can be analyzed by fitting the analytical homogeneous solution for the linear problem (i.e., normal modes) as a function of time as in Shimizu et al. (2007); this is equivalent to using an energy spectrum to capture the energy fluxes between different wave numbers (Maxworthy 1983; Melville et al. 1989; Fedorov and Melville 2000). Mathematically, it is possible to express every wave in a convergent series of linear modes (Shimizu et al. 2007). However, for the series expansion to retain its physical meaning, the series was terminated when the length scale reduced to that of the solitary-type waves. As seen in Fig. 7, as the solitary-type waves steepened, their amplitude increased and their length scale decreased; clearly this means that the series fit will need to be terminated so that the basin-scale waves and the solitary-type waves remain separate.

As a first step, consider the estimate of the amount of energy contained in such solitary-type waves. The energy per soliton and per unit of width (radius) along r was obtained from the theoretical solution of the KdV equation (Boegman et al. 2005b) as a function of the soliton amplitude. This energy was then summed over the observed train of solitons obtained in the simulation. The energy per soliton (TEs) is given by
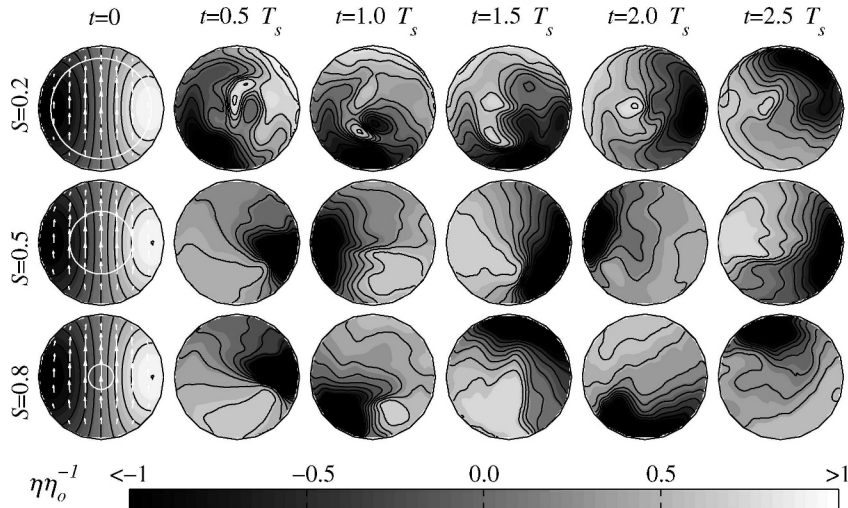

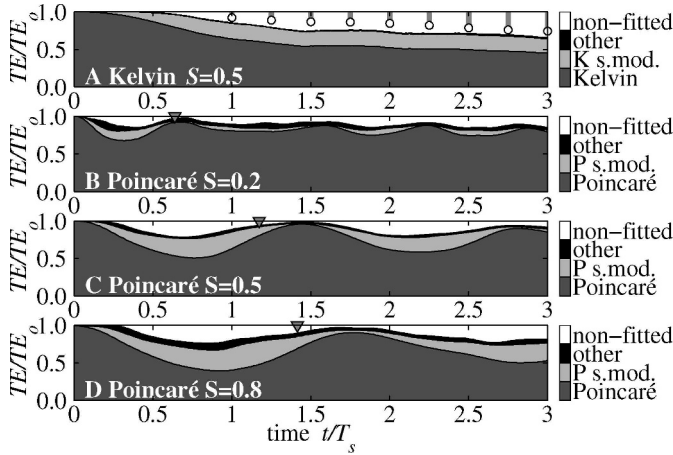Fig. 9. Same as Fig. 7 but for an initial monochromatic Poincaré wave.

Fig. 10. Time series of fitted modal energy nondimensionalized by the total energy of the simulation. (A) An initial Kelvin wave case with $S = 0.5$ and (B–D) initial Poincaré wave cases with $S = 0.2$, 0.5, and 0.8, respectively. Dark gray corresponds to the leading wave (Poincaré or Kelvin), light gray the higher azimuthal modes of the leading wave, black the energy contained in other basin-scale modes (radial and azimuthal), and white the other components that approximately corresponds to solitary-type waves. White dots in the upper panel correspond to the estimated energy of the solitons (*see* text) measured as is seen in the gray bars. Triangles in panels B–D indicate the period of the leading Poincaré waves.

$$\text{TEs} = c_0(\rho_2 - \rho_1)g \int\limits_0^{r_0} \int\limits_{\to \infty}^{\infty} \eta_2[a(r), t]^2 \, dt \, dr$$

$$(15)$$

$$\eta[a(r), t] = a(r)\,\text{sech}\left(\frac{c_0 t}{\lambda}\right)^2 \qquad \lambda^2 = 12\frac{\left(\bar{h}_1\bar{h}_2\right)^2}{\left(\bar{h}_2 - \bar{h}_1\right)a(r)}$$

where the amplitude $a(r)$ was obtained from the simulation results. The series expansion was then terminated at the number of modes that contained the residual energy equal to that in the train of solitons at a time equal to three steepening times; this required four higher azimuthal submodes of the Kelvin wave.

On the basis of the above criteria, the first 10 radial and the first four azimuthal modes of cyclonic and anticyclonic waves were fitted. The energies contained in the modes were grouped into four classes: leading wave (Kelvin or Poincaré), high azimuthal submodes of the leading wave (denoted in Fig. 10 as K s-mod. and P s-mod., respectively), other modes (denoted as other in Fig. 10), and the nonfitted energy that corresponds to residual energy. The energy contained in the solitary-type waves was also calculated by Eq. 15. Fig. 10 shows a typical time series of the total energy evolution, normalized by the total energy among the different categories for $W = 0.6$, $\bar{h}_1/\bar{h}_2 = 0.1$, and $S = 0.5$ for an initial Kelvin wave case (Fig. 10A) and $S = 0.2$, 0.5, and 0.8 for an initial Poincaré wave case (Fig. 10B–D, respectively). The energy evolution for the initial Kelvin wave was insensitive to S.
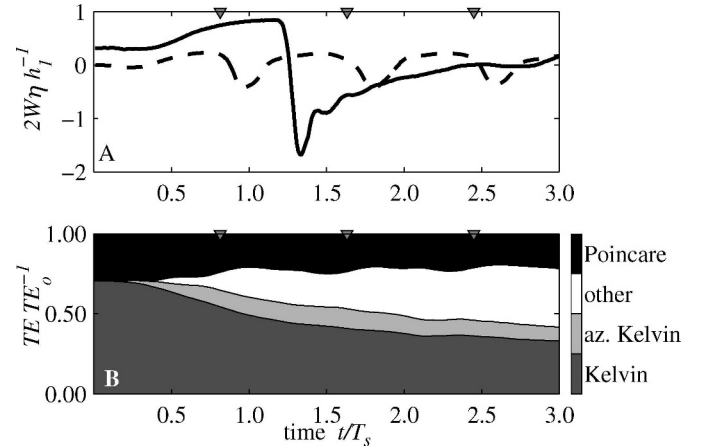

Fig. 11. (A) Time series of dimensionless interfacial displacement at the upwind end (solid line) and at the center of the basin (dashed line). (B) Time series of fitted modal energy nondimensionalized by the total energy of the simulation for $S = 0.5$, $W = \bar{h}_1(2\eta_0)^{-1} = 0.6$ and $\bar{h}_1/\bar{h}_2 = 0.1$. Triangles in upper axis mark T_{KP} period.

For the initial Kelvin wave case, the energy contained in the leading wave was mainly transferred to the submodes and the residual energy corresponding to energy contained in solitary-type waves (Fig. 10A). At $t = 3T_s$, the submodes and solitary-type waves had about 20% and 30% of the total energy, respectively (Fig. 10A). By contrast, for the initial Poincaré wave case (Fig. 10B–D), the energy was transferred into submodes, and then the transferred energy was observed to periodically return to the parent wave forming a limit cycle. The period of that interaction was about 1.2 times the natural period of the Poincaré wave for all the runs. The maximum energy transfer increases with the magnitude of S, being equal to about 30% of the total energy for $S = 0.2$, 50% of the total energy for $S = 0.5$, and 65% of the total energy for $S = 0.8$, indicating that rotation suppresses steepening of a Poincaré wave.

Coupling of free Kelvin and Poincaré waves—The nonlinear interactions between basin-scale waves was analyzed by initializing the simulation with the displacement and velocity field described by the linear superposition of a Kelvin and a Poincaré waves that were in phase. Their relative amplitudes were determined from the linear solution of the suddenly imposed wind problem at $t = (T_K - T_P)(T_K T_P)^{-1}$, where T_K and T_P are the periods of Kelvin and Poincaré waves, respectively. Time series of the interfacial displacements at the upwind end and at the center of the basin are shown in Fig. 11A for the cases $S = 0.5$, $W = 0.6$, and $\bar{h}_1/\bar{h}_2 = 0.1$. The energy decomposition into the leading Kelvin and Poincaré waves and the higher azimuthal Kelvin modes are shown in Fig. 11B.

The steepening and subsequent degeneration of the Kelvin wave into solitary-type waves was similar to the monochromatic Kelvin wave case (Fig. 11A); however, at the center of the basin, a standing oscillation with a period $T_{KP} = (T_K - T_P)(T_K T_P)^{-1}$ (*see* triangles in the upper axis in Fig. 11A) was excited when both the leading waves were

in phase. The excitation of this oscillation at the center of the basin explains that it was, in the suddenly imposed problem, due to nonlinear interaction of the Kelvin and Poincaré waves excited by the wind and not by the wind forcing itself.

The energy decomposition into modes shows the previously described pattern; that is, the energy in Kelvin waves were transferred to its subazimuthal modes and degenerated into solitary-type waves, whereas the energy contained in Poincaré waves remained available for a longer time. Nonlinear interaction between both waves transferred energy to the standing wave with a period of T_{KP}, which was then not recycled back to the Poincaré or Kelvin waves.

Triad nonlinear interaction was thought to explain the excitation of the T_{KP} standing wave (Phillips 1966). This nonlinear interaction occurs when three wave components satisfy the relationships $\omega_1 \pm \omega_2 \pm \omega_3 = 0$ and $k_1 \pm k_2 \pm k_3 = 0$, where ω_1, ω_2, and ω_3 are frequencies of the three waves and k_1, k_2, and k_3 are the corresponding wave numbers. The energy can be transferred among the wave components (Phillips 1966; Hammack and Henderson 1993). For the first-order problem, the governing equations for the lower layer are

$$\frac{\partial \eta_2^{(1)}}{\partial t} + h_2 \frac{\partial u_2^{(1)}}{\partial x} + h_2 \frac{\partial v_2^{(1)}}{\partial y} = -\eta_2^{(0)} \left(\frac{\partial u_2^{(0)}}{\partial x} + \frac{\partial v_2^{(0)}}{\partial y} \right)$$

$$\frac{\partial u_2^{(1)}}{\partial t} + \varepsilon_1 g \frac{\partial \eta_1^{(1)}}{\partial x} + \varepsilon_2 g \frac{\partial \eta_2^{(1)}}{\partial x} - f v_2^{(1)} = -u_2^{(0)} \frac{\partial u_2^{(0)}}{\partial x} - v_2^{(0)} \frac{\partial u_2^{(0)}}{\partial y} \quad (16)$$

$$\frac{\partial v_2^{(1)}}{\partial t} + \varepsilon_1 g \frac{\partial \eta_1^{(1)}}{\partial y} + \varepsilon_2 g \frac{\partial \eta_2^{(1)}}{\partial y} + f u_2^{(1)} = -u_2^{(0)} \frac{\partial v_2^{(0)}}{\partial x} - v_2^{(0)} \frac{\partial v_2^{(0)}}{\partial y}$$

where the superscripts (0) and (1) denote the leading waves and first-order perturbation that describe weak nonlinear effects. It is clear that the set of governing equations for the first-order approximation is the same as the linear case (the left-hand side of Eq. 16) but forced by the nonlinear interaction of the linear solution (the right-hand side of Eq. 16). The Kelvin–Poincaré interaction is at frequencies $\omega = [2\omega_K, 2\omega_P, \omega_K - \omega_P, \omega_K + \omega_P]$, where ω_K and ω_P are the natural frequencies of Kelvin and Poincaré waves, respectively. Because the basin is circular (so that natural frequencies do not occur in multiples of the fundamental frequency) and natural frequencies of the system remain the same as the linear waves, these forcing frequencies do not match with any of the natural frequencies. Therefore, the triad interaction is unlikely to be the excitation mechanism of the wave with a period of T_{KP}, even though the frequency relationship holds.

Another explanation investigated is that the observed oscillation, in the center of the basin, is simply a forced displacement and governed by Eq. 16. To show this, in Fig. 12, we plot the temporal average of the energy (within $t = 0$ and $3T_s$) contained in the fitted modes against frequency with both variables being obtained from the modal decomposition shown in Figs. 10A,C, 11B. The
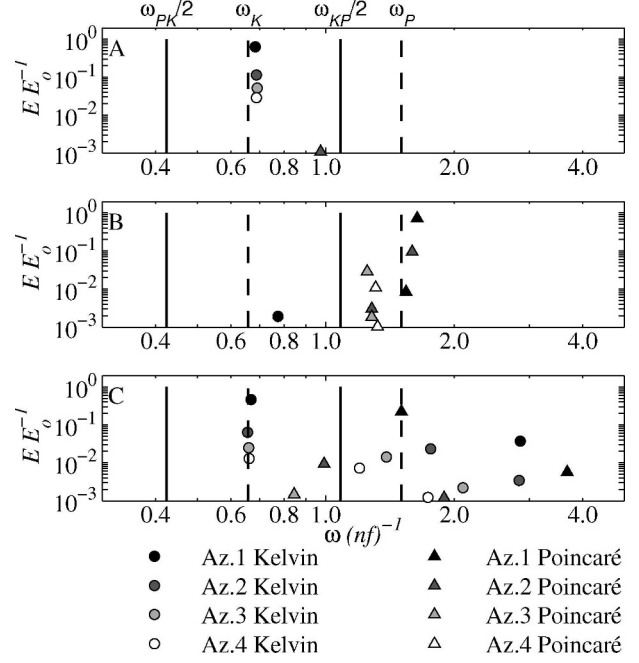

Fig. 12. Temporal average of the fitted energies of an initial Kelvin wave (as in Fig. 10A), an initial Poincaré wave (Fig. 10C) and an initial superposition of both waves (Fig. 11B), all for $S = 0.5$, as a function of the computed frequencies on the fitting. Circles denote cyclonic waves, triangles denote anticyclonic waves, and shading indicates azimuthal modes. Marked frequencies are for pure Kelvin and Poincaré waves (ω_K and ω_P, respectively), and $\omega_{KP}/2 = (\omega_K - \omega_P)/2$ and $\omega_{PK}/2 = (\omega_K + \omega_P)/2$.

horizontal axis of Fig. 12 is the frequency ω, of fitted linear mode, normalized by f and divided by the azimuthal order n. Division by the modal number highlights whether the higher azimuthal modes are locked to the Kelvin, Poincaré, or forcing frequencies, $\omega_{KP} = \omega_K - \omega_P$ and $\omega_{PK} = \omega_K + \omega_P$. A mode is locked by another one when both angular velocities are equal. For example, the frequency of an azimuthal mode 2 locked by the Kelvin wave, has twice the Kelvin wave frequency and is its subharmonic. It is seen from Fig. 12 that the observed frequencies of the azimuthal mode 2 waves are almost equal to the forcing frequency, explaining why, in Fig. 12, the frequencies ω_K, ω_P, $\omega_{KP}/2$, and $\omega_{PK}/2$ are marked as forcing frequencies.

For a monochromatic Kelvin wave, the case shown in Fig. 12A, we see that the azimuthal subharmonics of the leading Kelvin wave are locked by the leading Kelvin wave as the parent waves steepens. Through this representation it is clear that all frequencies belong to the parent wave and its subharmonics. A similar result was obtained for the monochromatic Poincaré wave, the results for which are shown in Fig. 12B with $S = 0.5$. The frequencies of the first two anticyclonic radial modes and their respectively azimuthal submodes again belong to or are near the leading Poincaré wave. A linear combination of Kelvin and Poincaré waves gave rise to subharmonics of both the parent Kelvin and Poincaré waves, as seen in Fig. 12C, but also energy was observed at other frequencies. The exact nature of these waves remains uncertain. That the observed

frequencies were not distinctively different from the natural frequencies suggests that the remaining energy, as represented by these non-subharmonic waves, was merely the manifestation of the nonlinear departure of the interface displacements and thus an artifact of the modal least squares fitting.

Discussion

Helfrich (2007) showed that an initial perturbation of the form of solitons in a nonrotating fluid first degenerates by radiating longer inertia-gravity waves that resteepen to form new solitary-type waves that decay and reemerge periodically. These observations are somewhat similar to what was described above for Poincaré waves. For Kelvin waves, our results are even more similar to those for a nonrotating fluid, as shown by Renouard (1986), who observed degeneration of Kelvin waves into solitary-type waves that had a squared hyperbolic secant profile in a rotating channel. The effect of rotation only modified the transverse interface gradient and did not influence the degeneration processes.

In previous research, two major groups of mechanism for the damping of the basin-scale internal waves have been identified: shear stress at the benthic boundary layer (Wüest et al. 2000; Marti and Imberger 2006) and nonlinear energy transfer into the high-frequency waves, which radiate toward the boundary where they break on a sloping bottom (Horn et al. 2001; Boegman et al. 2003; Boegman et al. 2005a). Interior dissipation because of, for instance, shear instabilities, is small relative to these effects and can be neglected (Wüest et al. 2000).

The mechanisms of degeneration into high-frequency waves have been investigated for nonrotating basins (Horn et al. 2001), wherein the magnitude of the perturbation, W, and the ratio $\bar{h}_1/\bar{h}_2$ were used as the parameters to characterize the degeneration processes. Different studies conjectured that rotation would reduce the relative importance of the formation of solitary waves. Solitary waves of permanent form, as obtained for nonrotating flows (Grimshaw et al. 1998; Ostrovsky and Stepanyants 2005; Helfrich and Melville 2006), were unknown for rotating flows. However, field measurements have clearly shown the presence of solitary-type high-frequency waves in rotating lakes, whose features can be explained on the basis of the nonrotating theory (Boegman et al. 2003; Appt et al. 2004). The degeneration processes described in this paper provide an explanation for their presence, showing that, for timescales $<3T_s$, the evolution of the Kelvin wave can be likened to a nonrotating long wave. A graphic example of such waves, arising from Kelvin waves is described in Appt et al. (2004) from observations in Upper Lake Constance.

The inclusion of both nonlinear and nonhydrostatic accelerations, when describing the response of a stratified rotating lake, has shown that Kelvin waves quickly lose their energy to subazimuthal modes and solitary-type waves. By contrast, Poincaré waves do not lose much energy to other modes or high-frequency waves but rather exhibit a limit cycle behavior where energy is transferred back and forth between the parent wave and its azimuthal subharmonics. If a Kelvin and Poincaré wave co-exist in a lake they become coupled and give rise to the same azimuthal subharmonics, but in addition, energy is drained into distortion of the interface because of nonlinearities.

References

ANTENUCCI, J. P., AND J. IMBERGER. 2001. Energetics of long internal gravity waves in large lakes. Limnol. Oceanogr. **46:** 1760–1773.

———, ———, AND A. SAGGIO. 2000. Seasonal evolution of the basin-scale internal wave field in a large stratified lake. Limnol. Oceanogr. **45:** 1621–1638.

APPT, J., J. IMBERGER, AND H. KOBUS. 2004. Basin-scale motion in stratified Upper Lake Constance. Limnol. Oceanogr. **49:** 919–933.

BAINES, P. G. 1998. Topographic effects in stratified flows. Cambridge Univ. Press.

BENNETT, J. R. 1973. A theory of large amplitude Kelvin wave. J. Phys. Oceanogr. **3:** 57–60.

BOEGMAN, L., J. IMBERGER, G. N. IVEY, AND J. P. ANTENUCCI. 2003. High-frequency internal waves in large stratified lakes. Limnol. Oceanogr. **48:** 895–919.

———, G. N. IVEY, AND J. IMBERGER. 2005a. The degradation of internal waves in lakes with sloping topography. Limnol. Oceanogr. **50:** 1620–1637.

———, ———, AND J. IMBERGER. 2005b. The energetics of large-scale internal wave degeneration in lakes. J. Fluid Mech. **531:** 159–180.

BRADFORD, S., N. KATOPOES, AND G. PARKER. 1997. Characteristic analysis of turbid underflows. J. Hydrol. Eng. **123:** 420–431.

BRANDT, P., A. RUBINO, W. ALPERS, AND J. O. BACKHAUS. 1997. Internal waves in the stair of Messina studied by numerical model and synthetic aperture radar images from the ERS 1/2 satellites. J. Phys. Ocenogr. **27:** 648–663.

CHOI, W., AND R. CAMASSA. 1999. Fully nonlinear internal waves in two-fluid system. J. Fluid Mech. **396:** 1–36.

CLARK, S. R., AND J. IMBERGER. 1996. Nonlinear effects in the unsteady, critical withdrawal of a stratified fluid. Dyn. Atmos. Oceans **24:** 163–171.

CSANADY, G. T. 1968. Motions in a model Great Lake due to suddenly imposed wind. J. Geophys. Res. **73:** 6435–6447.

———. 1973. Transverse internal seiches in large oblong lakes and marginal seas. J. Phys. Oceanogr. **3:** 439–447.

DE LA FUENTE, A., Y. NIÑO, R. MUÑOZ, AND R. FREDERICK. 2006. By *n*-layers, a 2D multilayers model for natural stratified flows. VIth International Symposium of Stratified Flows. Perth, Australia, 667–672.

FEDORONOV, A., AND W. K. MELVILLE. 2000. Kelvin front on the equatorial thermocline. J. Phys. Oceanogr. **30:** 1692–1705.

FEDOROV, A., AND W. K. MELVILLE. 1995. Propagation and breaking of nonlinear Kelvin wave. J. Phys. Oceanogr. **25:** 2518–2531.

FISCHER, H., E. LIST, R. KOH, J. IMBERGER, AND N. BROOKS. 1979. Mixing in inland and coastal waters. Academic.

GILL, A. E. 1982. Atmosphere–ocean dynamics. Academic.

GÓMEZ-GIRALDO, A., J. IMBERGER, AND J. P. ANTENUCCI. 2006. Spatial structure of the dominant basin-scale internal waves in Lake Kinneret. Limnol. Oceanogr. **51:** 229–246.

GRIMSHAW, R. H. J., L. A. OSTROVSKY, V. I. SHRIRA, AND Y. A. STEPANYANTS. 1998. Long nonlinear surface and internal gravity waves in a rotating ocean. Surv. Geophys. **19:** 289–338.

HAMMACK, J. L., AND D. M. HENDERSON. 1993. Resonant interactions among surface water waves. Annu. Rev. Fluid Mech. **25:** 55–97.

HEAPS, N. S., AND A. E. RAMSBOTTOM. 1966. Wind effects in the water in a narrow two layered lake. Phil. Trans. R. Soc. Lond. A **259:** 391–439.

HELFRICH, K. 2007. Decay and return of inertial solitary waves with rotation. Phys. Fluids. **19:** 026601, doi: 10.1063/1.2472509.

———, AND W. MELVILLE. 2006. Long nonlinear internal waves. Annu. Rev. Fluid Mech. **38:** 395–425.

HORN, D., J. IMBERGER, AND G. N. IVEY. 2001. The degradation of long-scale interfacial gravity waves in lakes. J. Fluid. Mech. **434:** 181–207.

———, ———, ———, AND L. G. REDEKOPP. 2002. A weakly nonlinear model of long internal waves in close basins. J. Fluid. Mech. **467:** 269–287.

IMBERGER, J. 1998. Flux path in a stratified lake: A review, p. 1–17. *In* J. Imberger [ed.], Physical processes in Lakes and Oceans. American Geophysical Union.

———, AND P. HAMBLIN. 1982. Dynamics of lakes, reservoirs, and cooling ponds. Annu. Rev. Fluid Mech. **14:** 153–187.

LEE, C.-Y., AND R. C. BEARDSLEY. 1974. The generation of long nonlinear internal waves in a weakly stratified shear flow. J. Geophys. Res. **79:** 453–462.

LOOSE, B., Y. NIÑO, AND C. ESCAURIAZA. 2005. Finite volume modelling of variable density shallow-water equations for a well-mixed estuary: Application to the Río Maipo estuary in central Chile. J. Hydr. Res., **43:** 339–350.

MARTI, C., AND J. IMBERGER. 2006. Dynamics of the benthic boundary layer in a strong forced stratified lake. Hydrobiologia **568:** 217–233.

MAXWORTHY, R. 1983. Experiments in solitary internal Kelvin waves. J. Fluid Mech. **129:** 365–383.

MELVILLE, W. K., G. G. TOMASSON, AND D. P. RENOUARD. 1989. On the stability of Kelvin waves. J. Fluid Mech. **206:** 1–23.

MONISMITH, S. G. 1985. Wind-induced motions in stratified lakes and their effect on mixed-layer shear. Limnol. Oceanogr. **30:** 771–783.

MORTIMER, C. H. 1952. Water movement in lakes during summer stratification; evidence from the distribution of temperature in Windermere. Phil. R. Soc. Lond. Ser B. **236:** 355–398.

MUNNICH, M., A. WÜEST, AND D. M. IMBODEN. 1992. Observations of the second vertical mode of the internal seiche in and alpine lake. Limnol. Oceanogr. **37:** 1705–1719.

OSTROVSKY, L. A., AND Y. A. STEPANYANTS. 2005. Internal solitons in laboratory experiments: Comparison with theoretical models. Chaos **15:** 1–28.

PHILLIPS, O. M. 1966. The dynamics of the upper ocean. Cambridge Univ. Press.

RENOUARD, D., D. CHABERT, AND X. ZHANG. 1986. An experimental study of strongly nonlinear waves in a rotating system. J. Fluid Mech. **177:** 381–394.

RILEY, J. J., AND M. P. LELONG. 2000. Fluid motion in the presence of strong stable stratification. Annu. Rev. Fluid Mech. **32:** 613–657.

RIPA, P. 1982. Nonlinear wave–wave interactions in a one-layer reduced-gravity model on the equatorial β plane. J. Phys. Oceanogr. **12:** 97–111.

SHIMIZU, K., J. IMBERGER, AND M. KUMAGAI. 2007. Horizontal structure and excitation of primary motion in a strongly stratified lake. Limnol. Oceanogr. **52:** 2641–2655.

SPIGEL, R. H., AND J. IMBERGER. 1980. The classification of mixed layer dynamics in lakes of small to medium size. J. Phys. Oceanogr. **10:** 1104–1121.

STOCKER, R., AND J. IMBERGER. 2003. Energy partitioning and horizontal dispersion in a stratified rotating lake. J. Phys. Oceanogr. **33:** 512–529.

THOMPSON, R., AND J. IMBERGER. 1980. Response of a numerical model of a stratified lake to wind stress. IIth International Symposium of Stratified Flows. Trondheim, Norway.

TOMASSON, G. G., AND W. K. MELVILLE. 1992. Geostrophic adjustment in a channel: nonlinear and dispersive effects. J. Fluid Mech. **241:** 23–57.

WÜEST, A., AND A. LORKE. 2003. Small-scale hydrodynamics in lakes. Annu. Rev. Fluid Mech. **35:** 373–412.

———, G. PIEPKE, AND D. VAN SENDEN. 2000. Turbulent kinetic energy balance as a tool for estimating vertical diffusivity in wind-forced stratified waters. Limnol. Oceanogr. **45:** 1388–1400.